Metallophysics and Advanced Technologies
Металофіз. новітні технол.
Metallofiz. Noveishie Tekhnol.
2024, vol. 46, No. 10, pp. 991–1005
https://doi.org/10.15407/mfint.46.10.0991
Reprints available directly from the publisher

PACS numbers: 46.50.+a, 46.55.+d, 61.72.Ff, 62.20.Qp, 68.35.Ct, 68.37.Hk, 81.40.Pq

Comparative Tribological Analysis of Al–Fe–Si-Based Alloys

Haidar Faisal Helal Mobark, Ali Hussein Al-Azzawi*, Mothanna Taha Mohammed Fattah Agha, Abdulraheem Kadhim Abid Ali**, and Barhm Mohamad***

College of Agriculture, Department of Soil Sciences and Water Resources,
Al-Qasim Green University,
51001 Babel, Iraq
**College of Engineering, Department of Mechanical Engineering,*
University of Misan,
62001 Misan, Iraq
***College of Materials Engineering,*
University of Babylon,
51001 Babel, Iraq
****Department of Petroleum Technology, Koya Technical Institute,*
Erbil Polytechnic University,
44001 Erbil, Iraq

This study presents a comparative investigation of the tribological behaviour and microstructural characteristics of two different alloys, namely, 77.3% Al–1.8% Fe–16.7% Si (Al–Si-based alloy) and 62.9% Al–14.4% Fe–16.9% Si (Al–Fe–Si-based alloy). High temperature alloys are fabricated by stir-casting technique. Tribology analysis is conducted to assess wear, crack formation, and cavity zones for both alloys using scanning electron microscopy. In addition, optical micrography is used to examine their microstructures. The results reveal significant differences between the two alloys: with the high concentration, Si-alloy specimen exhibits higher Vickers hardness and superior wear resistance compared to the low-concentration Si-alloy specimen. Optical micrographs confirm a well-defined grain distribution for the former alloy and a similar homogeneous microstructure for the latter.

Key words: materials science, stir casting, alloys' fabrication, tribology anal-

Corresponding author: Haidar Faisal Helal Mobark
E-mail: mobark.mechanical@gmail.ua

Citation: Haidar Faisal Helal Mobark, Ali Hussein Al-Azzawi, Mothanna Taha Mohammed Fattah Agha, Abdulraheem kadhim AbidAli, and Barhm Mohamad, Comparative Tribological Analysis of Al–Fe–Si-Based Alloys, *Metallofiz. Noveishie Tekhnol.*, **46**, No. 10: 991–1005 (2024). DOI: 10.15407/mfint.46.10.0991

ysis, surface damage.

В роботі представлено порівняльне дослідження трибологічної поведінки та мікроструктурних характеристик двох різних стопів: 77,3% Al–1,8% Fe–16,7% Si (стоп на основі Al–Si) та 62,9% Al–14,4% Fe–16,9% Si (стоп на основі Al–Fe–Si). Високотемпературні стопи виготовлено методою лиття з перемішуванням. Трибологічну аналізу проведено методою сканувальної електронної мікроскопії для оцінки зносу, утворення тріщин і порожнин для обох стопів. Крім того, для дослідження їхньої мікроструктури було використано оптичну мікрографію. В результаті виявлено значні відмінності між двома стопами, причому зразок стопу з високою концентрацією Силіцію має вищу твердість за Віккерсом і більш високу зносостійкість порівняно зі зразком стопу з низькою концентрацією Силіцію. Оптичні мікрофотографії підтверджують чіткий розподіл зерен для першого стопу та подібну однорідну мікроструктуру для другого.

Ключові слова: матеріялознавство, лиття з перемішуванням, виготовлення стопів, трибологічна аналіза, пошкодження поверхні.

(Received 5 December, 2023; in final version, 9 July, 2024)

1. INTRODUCTION

Tribology, the study of friction, wear, and lubrication of materials, has garnered significant interest in recent years, especially in the context of Al–Fe–Si based alloys. These alloys are renowned for their excellent mechanical properties and potential applications in various industries. Their tribological behaviour has been the subject of extensive research, aimed at understanding their performance under different conditions.

Aluminium–silicon (Al–Si) alloys stand out as the most extensively utilized among the three types of cast aluminium alloys. These alloys demonstrate superior wear resistance, a low coefficient of thermal expansion, and excellent casting properties, including good fluidity, minimal shrinkage rate, and a reduced hot crack tendency [1–4]. Constituting 85–90% of all aluminium castings, Al–Si alloys play a pivotal role in moulding castings. In aerospace applications, these alloys find extensive use in electronic packaging materials, engine components, and various non-structural parts such as valve housings, turbine impellers, cooling fans, fixtures, rollers, pulleys, bucket bars, and manifolds. Notably, the representative A357 (Al–Si7–Mg) grade of Al–Si alloy is prominently employed in the body and fuel tank of the Alcoa AGM-86B cruise missile. The fuel tank comprises four large A357-T6 Al alloy castings, distinguished by their significant size, high precision, and complex shapes, constituting 80% of the projectile body, including components like the head cone, inertial navigation device cabin, engine inlet, conical wing, and various brackets [5].

Al–Si binary alloys, by nature, cannot be strengthened through heat treatment. To enhance their overall properties, alloying elements such as Mg, Mn, and Cu are commonly added, transforming the alloy into a heat-treatable and strengthened variant. Each element contributes distinct advantages and drawbacks; for instance, Cu improves heat resistance and tensile properties but may reduce casting and corrosion resistance. Meanwhile, Mg enhances mechanical strength and corrosion resistance but can compromise casting performance, and Mn forms compounds with Fe to enhance heat resistance. Conventional cast Al alloys often exhibit needle-like eutectic Si and coarse primary Si in their microstructure, leading to diminished strength and plasticity. Therefore, inoculants like Nb, B, Na, Sr, and Sb are frequently incorporated to refine the microstructure and enhance the comprehensive properties of Al–Si alloys [6, 7]. For instance, Bolzoni *et al.* (2015) introduced Nb–B inoculants to an Al–Si alloy, resulting in a significant reduction in the size of α-Al and eutectic phases, thereby improving mechanical properties. The yield strength (YS) of Al–Si alloys generally falls within the range of 150 to 350 MPa.

In comparison to Al–Si alloys, aluminium–copper (Al–Cu) cast alloys boast higher mechanical properties, improved cutting performance, high-temperature capabilities, and effective age hardening, attributed to the Al_2Cu reinforced phase. This makes them suitable for structural components operating at elevated temperatures or handling larger loads at room temperature. Among Al–Cu alloys, $AlCu_5MnCdV$ stands out for its high strength and plasticity, alloyed primarily with Cu, Mn, Ti, and trace elements Zr, Cd, V, and B. As one of the strongest Al–Cu alloys, $AlCu_5MnCdV$ finds extensive application in the aerospace sector, excelling in mechanical performance at both high and room temperatures, making it the preferred material for aircraft frame components [8].

Aluminium–magnesium (Al–Mg) cast alloys are characterized by excellent corrosion resistance, weldability, moderate strength, and high ductility. Among them, $AlMg_5Si_1Mn$, incapable of strengthening through heat treatment, is widely employed in aerospace applications due to its exceptional weldability and heat resistance. This alloy is commonly used in aircraft engines, missiles, internal combustion engines, chemical pumps, petrochemical pump shells, rotors, blades, and other critical components [9, 10]. Researchers have explored the effects of alloy composition, heat treatment, and microstructural characteristics on friction and wear properties. Additionally, surface engineering techniques, such as coatings and treatments, have been investigated to enhance the tribological performance of these alloys.

Bharath *et al.* [11] conducted experiments on synthesizing Al2014 alloy reinforced with 20 μm Al_2O_3 particles and studying their microstructure and wear behaviour. They employ a two-stage stir casting

technique with varying weight percentages of reinforcement (9%, 12%, and 15%). Characterization using XRD and electron microscopy shows uniform dispersion of Al_2O_3 in the matrix. Wear tests reveal that both frictional coefficient and wear rate increase with load and sliding speed. Electron microscopy and EDS analysis identify oxide formation on worn surfaces, aiding in understanding wear mechanisms.

Kaiser *et al.* [12] explored the impact of Fe, Ni, and Cr additions on the wear behaviour of hypereutectic Al–Si automotive alloy. They conducted dry sliding wear tests under specific conditions. Fe addition increased wear rate due to needle-like intermetallic formation, while Ni showed no significant effect on microstructure. Cr addition transformed intermetallics into modified alpha phases, improving alloy strength and wear properties. Scanning electron microscopy (SEM) analysis revealed Cr-added alloy exhibited improved wear resistance with smooth abrasive grooves filled with oxides. A study conducted by Chouki Farsi *et al.* [13] focused on the application of a high-gradient magnetic separation method for the effective separation of weakly magnetic particles, specifically in an industrial setting.

The researchers explored and implemented high-gradient magnetic separation techniques to address the challenges of separating weakly magnetic particles from complex mixtures in an industrial context. The study likely involved designing and testing a specialized magnetic separator to achieve efficient separation of these particles, which have relatively low magnetic susceptibility compared to strongly magnetic materials. The application of this method could have practical implications in various industries where precise separation of weakly magnetic particles is essential for processing and product quality. The study presented experimental results, data analysis, and insights into the performance and efficiency of the high-gradient magnetic separation method.

Al-Abboodi *et al.* [14] presents an evaluation of the mechanical properties of a metallic glass alloy ($Fe_{49.7}Cr_{17.1}Mn_{1.9}Mo_{7.4}W_{1.6}B_{15.2}C_{3.8}Si_{2.4}$) prepared by spark plasma sintering using a three-point bending apparatus. The study achieved notch fracture toughness and Young's modulus values of 231 GPa and 4.91 $MPa{\cdot}m^{1/2}$, respectively, and found reliable results for Young's modulus using Vickers indentation measurements. The proposed method for examining micro-scale mechanical properties is applicable to samples with different compositions made by other means.

Aldeen *et al.* [15] investigates the effects of isothermal and isochronal ageing on N36 zirconium alloy after β-quenching. The research involves characterization using various microscopy techniques and spectroscopy to observe microstructure and second-phase particle (SPPs) evolution. The results reveal that the implemented quenching leads to a fine interlaced α-plates structure, and after ageing, recrystallization occurs with non-uniform grains and a random SPPs distribution.

Hardness declines with increasing temperature and time, while roughness and wettability increase with higher ageing temperatures.

Kang *et al.* [16] explores the fabrication of Al–Fe–Cr quasi-crystal-reinforced metal matrix composites using a laser powder bed fusion (LPBF) process. The LPBF-processed Al–Fe–Cr alloy exhibits a multiscale heterogeneous structure with nanosize Al–Fe–Cr quasi--crystalline particles distributed in the α-Al columnar grain structure. The alloy demonstrates high mechanical strength due to the ultrafine multireinforced microstructure-induced Orowan strengthening effect, resulting in an ultimate tensile strength of 530.80 MPa, yield strength of 395.06 MPa, and elongation of 4.16%. The fractographic analysis indicates a combination of ductile-brittle fracture as the dominant fracture mechanism.

Zhang *et al.* [17] focuses on a specially designed Al–Fe–Cr alloy fabricated through a laser powder bed fusion (LPBF) process, resulting in a multiscale heterogeneous composite structure with high relative density and defect-free features. The LPBF-processed sample exhibits distinct composite structures in three regions: the inner laser fusion zone (LFZ) with ultrafine cellular structures containing spherical Al–Fe–Cr quasi-crystals, the molten pool boundary (MPB) with coarse flower-like quasi-crystal particles and rectangular θ-$Al_{13}(Fe,Cr)_{2-4}$ particles, and the heat-affected zone (HAZ) with finer reinforcements dispersed in the α-Al matrix. The tribological investigation shows the LPBF-processed sample has stable friction coefficients and higher wear resistance compared to other LPBF-processed Al alloys, with a duplex wear mechanism of adhesive and oxidation wear.

Byron Blakey-Milner *et al.* [18] presented thorough review of metal additive manufacturing in the aerospace industry, highlighting its significant commercial and performance advantages. The opportunities in this field include cost and lead-time reductions, novel materials and unique design solutions, mass reduction through lightweight designs, and consolidation of components for improved performance and risk management. Various high-profile aerospace applications, such as rocket engines, propellant tanks, heat exchangers, turbomachinery, and satellite components, have already commercially benefited from metal additive manufacturing. The paper also addresses challenges and potential opportunities for using this technology in each application scenario.

Leyson *et al.* [19] presents a quantitative, parameter-free model for predicting the flow stress of alloys containing substitutional solutes. The model utilizes density functional theory and a flexible-boundary-condition method to describe accurately the interaction energies between solutes and dislocations. It successfully predicts flow stresses for various Al alloys, including Al–Mg and Al–Mn, and agrees well with experimental results for quasi-binary Al–Cr–(Fe) and Al–Cu–(Fe) alloys. The model offers a basis for computational design of alloys, fo-

cusing on solute-strengthening mechanisms, and aligns with the 'stress equivalency' postulate by Basinski.

In the study by Xi *et al.* [20], near-fully dense Al–12Si matrix composites reinforced with TiB_2 ceramic particles (2% wt.) were successfully fabricated using selective laser melting (SLM) and hot pressing (HP) techniques. The TiB_2 ceramic particles were homogeneously distributed in the Al–12Si matrix at the micrometer-scale due to excellent wetting between the molten alloy and ceramic. The microstructural analysis of the as-fabricated SLM samples showed the formation of a supersaturated α-Al phase and the decrease of free residual Si compared to the hot-pressed ones. Both composites exhibited a fine microstructure with a grain size of $\cong 5.1$ μm and $\cong 5.8$ μm for SLM and HP fabricated samples with addition of TiB_2 ceramic particles. The SLM Al–12Si/TiB_2 composite exhibited significantly improved microhardness ($\cong 142 \pm 6.0 HV_{0.05}$) and yield strength ($\cong 247 \pm 4.0$ MPa) compared to the corresponding HP one, attributed to the fine cell morphology and nanostructured dispersion strengthening achieved through the SLM process.

Kang *et al.* [21] fabricated Al–Fe–Cr quasi-crystal (QC) reinforced Al-based metal matrix composites through SLM from a powder mixture. Parametrical optimization focused on laser scanning speed, resulting in an almost dense (99.7%) free-crack sample with an ultra-fine microstructure. A phase transition from decagonal QC $Al_{65}Cu_{25}Fe_{10}Cr_5$ to icosahedral QC $Al_{91}Fe_4Cr_5$ is observed at lower laser scanning speeds. Differential scanning calorimetry curves revealed the QC phase stability up to 500°C. The study examined the effects of annealing temperature on the microstructural and mechanical properties, indicating that QC particles prevent α-Al grain recrystallization and growth during annealing. However, the growth of QC particles results in a porous structure, improving Young's modulus but reducing ductility.

In Ref. [22], an Al–1Fe (% wt.) alloy with nanosize Al_3Fe phase underwent continuous rheoextrusion and heat treatment. The nanosize phase was spheroidized during heat treatment, while coarsening and forming plate-like structures occurred with prolonged treatment. Tensile strength decreased slightly at 200° and 300°, but significantly at higher temperatures. However, the alloys' strength remained higher than the as-cast Al–Fe alloy throughout heat treatment.

Mahdi Khadem *et al.* [23] presented a review on multilayer coating systems for tribological applications. These coatings have been widely used to reduce friction and wear in mechanical systems, contributing to improved efficiency, reliability, and system lifespan. The paper focused on Ti-based and Cr-based coatings, exploring their materials, design concepts, mechanical properties, deposition methods, and friction and wear characteristics. Multilayer coatings offer the advantage of tailoring coating properties to suit specific operating conditions, making them highly versatile in various engineering applications. Al-

uminium alloys are essential materials in additive manufacturing (AM), but they face challenges due to low laser absorption, high thermal conductivity, and reduced powder flowability resulting in poor processability. Recent efforts have focused on developing new compositions specifically designed for laser-based powder bed AM.

The review by Alberta Aversa *et al.* [24] provides an overview of the state of the art, including microstructural and mechanical characterizations of these aluminium alloys used in laser powder bed fusion. Kotadia *et al.* [25] discuss the growing interest in AM of metallic alloys for structural and functional applications, revolutionizing design and manufacturing. While Ti- and Ni-based alloys have made rapid progress in AM, the development of AM with Al-alloys has been slower, despite their wide industrial adoption for their low density and high strength-to-weight ratio. The review focuses on microstructural characteristics, their influence on mechanical properties, and recent research on overcoming challenges associated with high-strength wrought Al alloys in AM. The paper highlights the promising advancements in understanding microstructure and defect formation, along with potential microstructural modification methodologies, while acknowledging the remaining challenges in this field.

Therefore, with the aim of obtaining high mechanical properties, wear resistance and low-cost Al–Fe–Si alloys, this study presents a comparative investigation of the tribological behaviour and microstructural characteristics of two different alloys, namely 77.3% Al–1.8% Fe–16.7% Si and 62.9% Al–14.4% Fe–16.9% Si.

2. EXPERIMENTAL TECHNIQUES

Sample Preparation. The Al–Fe–Si and Al–Si based alloys of samples were meticulously prepared by controlling the alloy composition. Stir casting techniques were used to fabricate the desired alloy, followed by heat treatment to achieve the desired microstructure and mechanical properties. The experimental data obtained from different tests as shown in Fig. 1 were subjected to rigorous statistical analysis. This comprehensive analysis allowed for comparisons between samples (Al–Fe–Si) and (Al–Si) alloys in different concentrations, and testing conditions, enabling the identification of significant trends and correlations.

3. DATA ANALYSIS

3.1. Microstructural Analysis

Comprehensive microstructural analysis was conducted using advanced techniques such as optical micrograph, SEM and wavelength dispersive

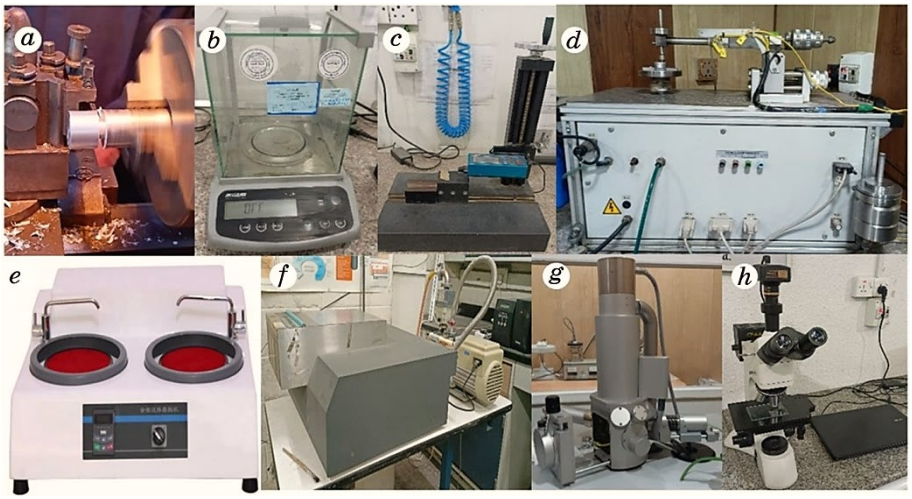

Fig. 1. Turing machine section to prepare specimen (*a*), microbalance GR 120 $d = 0.1$ mg capacity (*b*), surface roughness tester (*c*), microtest machine (*d*), grinder polisher (*e*), wavelength dispersive XRF spectrometer (*f*), scanning electron microscope (*g*), optical micrograph (*h*).

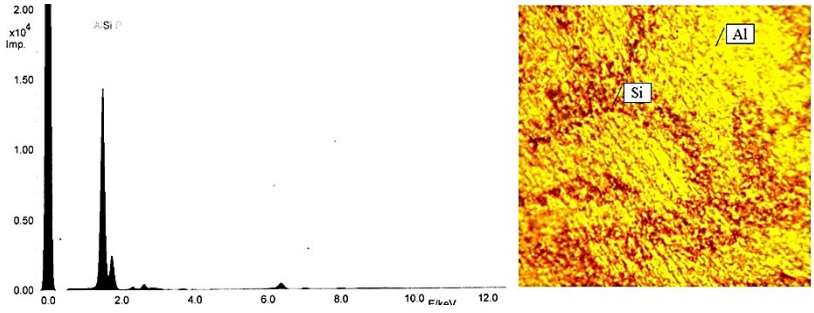

Fig. 2. Optical micrograph of microstructure of Al–Si-alloy specimen.

(XRF) spectrometer. This analysis provided valuable insights into the crystallography and microstructural features of the alloy, offering an understanding of their influence on tribological behaviour.

The optical micrographs of the Al–Si alloy as shown in Fig. 2 revealed important details about its internal microstructure and the presence of various phases, such as aluminium, iron, and silicon phases, contributed to the alloys. The optical micrographs showed the arrangement and size of the grains in the alloy. The grains appeared to have a well-defined and uniform distribution, suggesting a relatively homogenous microstructure. The presence of distinct grain boundaries indicated the formation of individual grains during the alloys solidification process.

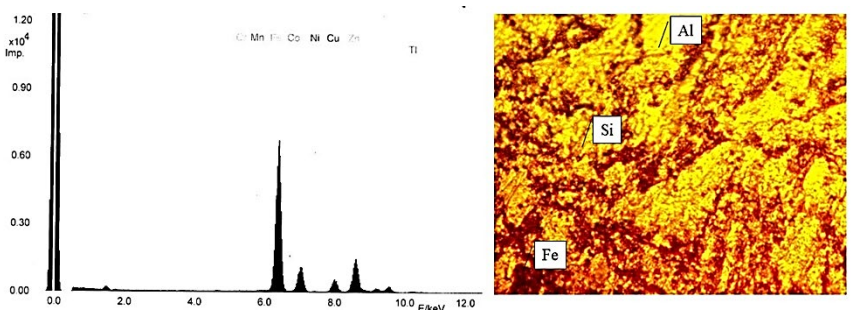

Fig. 3. Optical micrograph of microstructure of Al–Fe–Si-alloy specimen.

The microstructure for the Al–Fe–Si alloy will provide valuable information for comparison with the Al–Si alloy. In Figure 3, the arrangement and size of the grains in the Al–Fe–Si alloy are revealed. The grains appeared to have a defined and uniform distribution, indicating a reasonably homogeneous microstructure. The presence of distinct grain boundaries indicated the formation of individual grains during the alloys solidification process. The presence of various phases, such as aluminium, iron, and silicon phases, contributed to the alloys overall properties and behaviour.

3.2. Hardness Testing

To assess the materials resistance to deformation, hardness measurements were carried out using the Vickers or Rockwell hardness testing. These measurements provided crucial information related to the alloy's wear resistance. Figure 4 revealed that the Al–Fe–Si alloy exhib-

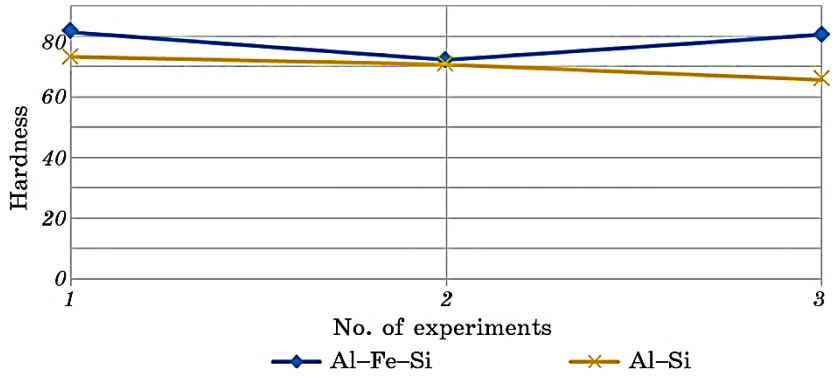

Fig. 4. Vickers hardness values for the Al–Fe–Si-alloy and Al–Si-alloy specimens.

TABLE 1. Standard deviation of specimens.

Specimens	σ
Al–Fe–Si	4.1332
Al–Si	3.0735

TABLE 2. The hardness and physical characteristics of the counterpart balls [26].

Counterpart	Vickers hardness, GPa	Roughness *Ra*, mm
316L	2	0.01
SiC	28	0.01
Al_2O_3	18	0.01
Fe–23Al–3Cr	3.49	0.2

ited higher Vickers hardness values compared to the Al–Si alloy, with a difference of approximately 20 degrees between the two specimens.

The standard deviation formula can be used to appraise the uniformity or dispersion of Vickers hardness values from a set of height or depth measurements. It is can be calculated using the standard deviation formula:

$$\sigma = \sqrt{\frac{1}{n}\sum_{j=1}^{n}(x_i - \mu)^2}\ , \tag{1}$$

where σ indicating the standard deviation, x_i represents each value in the data set and μ the mean of all the values within that data set, n is the number of values in the data set. Table 1 illustrates the standard deviation for each alloy specimen.

Zhang *et al.* [26] conducted the friction and wear tests using a ball-disk reciprocating frictional tester. The samples underwent polishing with a diamond grind for the tribological test. The counterpart balls included commercial 316L stainless steel, Al_2O_3, and SiC balls, with their respective hardness and associated parameters detailed in Table 2.

3.3. Tribometer Testing

Tribometer testing was performed under controlled conditions to study the friction and wear behaviour. Different tribometer setups, such as pin-on-disk, were utilized, varying the loads, sliding speeds, and lubrication conditions. The results demonstrated that the Al–Fe–Si alloy exhibited lower weight loss for all three test loads (3 N, 5 N, and 10 N), whereas the Al–Si alloy experienced higher weight loss un-

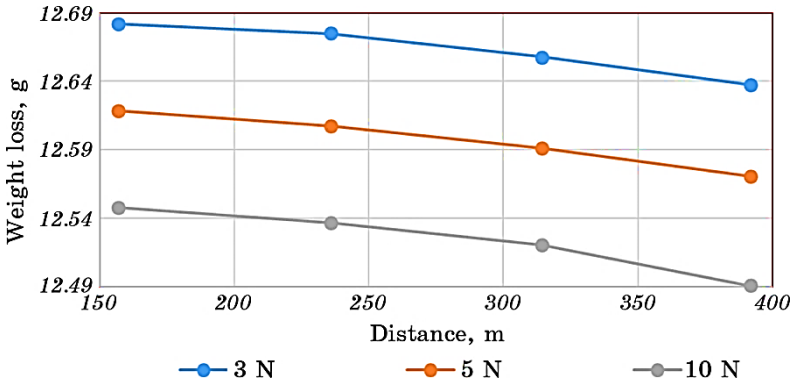

Fig. 5. Circular wear test for the Al–Si-alloy specimen.

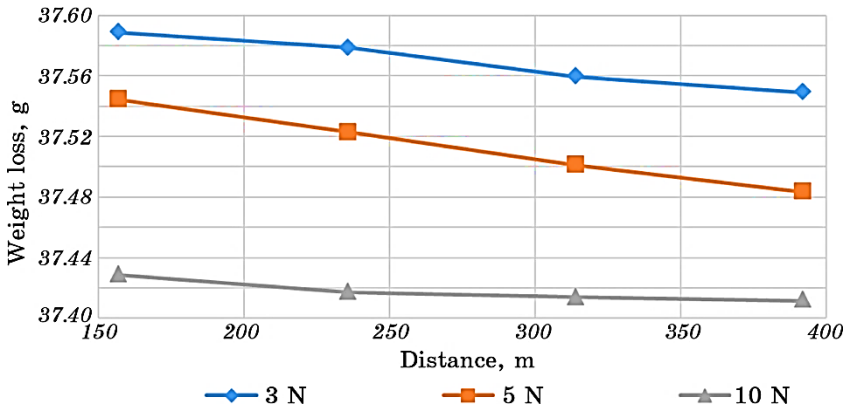

Fig. 6. Circular wear test for the Al–Fe–Si-alloy specimen.

der the same testing conditions, as shown in Figs. 5 and 6.

3.4. Surface Roughness Test

In addition to the base alloys testing, researchers explored surface engineering techniques. Surface roughness tests were performed on the Al–Fe–Si alloy and Al–Si alloy specimen, and the results indicated that the Al–Fe–Si alloys had higher surface roughness values, while the Al–Si alloys exhibited lower and more stable roughness levels as shown in Table 3.

3.5. Scanning Electron Microscopy (SEM)

The SEM images provided valuable information about the microstruc-

TABLE 3. Roughness value *Ra* for the Al–Fe–Si-alloy and Al–Si-alloy specimens.

Nos. of experiments	Al–Fe–Si alloy *Ra*, mm	Al–Si alloy *Ra*, mm
1	0.108	0.876
2	0.118	0.202
3	0.095	0.237

ture of the alloy, showing the arrangement and size of grains. The presence of different phases and grain boundaries can influence the alloys mechanical properties, such as hardness and strength.

The SEM images in Fig. 7 revealed distinct wear patterns on the alloys' surfaces. These wear features included abrasion marks, grooves, and microfractures, indicating the effects of frictional forces during the tribological tests. The wear resistance of the alloy appeared to be promising, as it showed limited wear damage and maintained its integrity under the specific test conditions. In addition, the analysis allowed for the detection and characterization of small cracks that had formed on the surface of the alloy. These cracks might have resulted from cyclic loading or localized stress concentration during the tribological tests. The presence of such microcracks did not seem to compromise the overall structural integrity of the alloy.

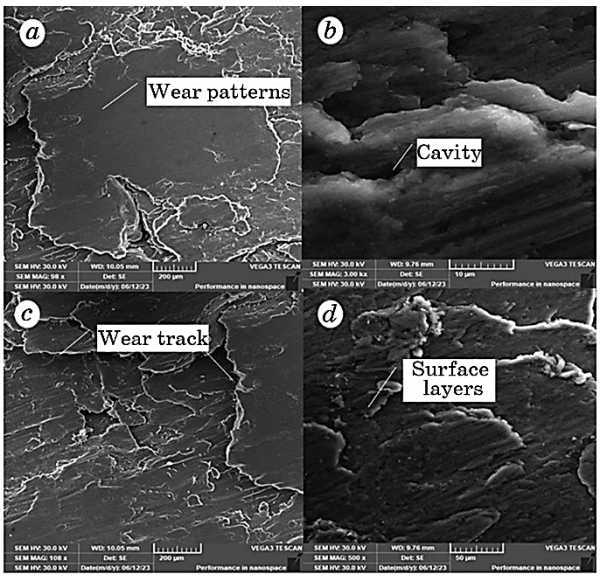

Fig. 7. The microstructure of Al–Si-alloy specimen revealed by scanning electron microscope.

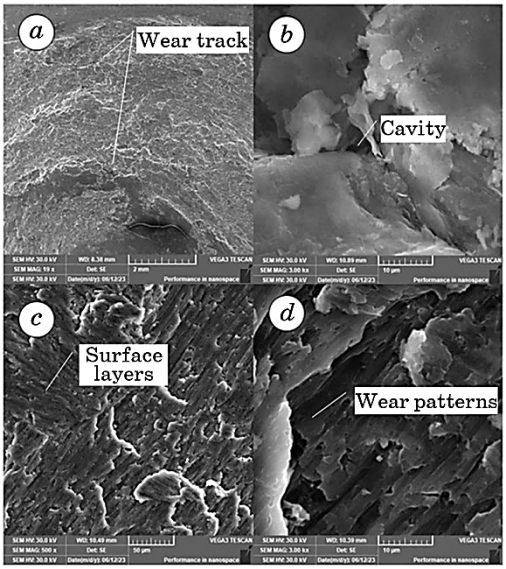

Fig. 8. The microstructure of Al–Fe–Si-alloy specimen revealed by scanning electron microscope.

The SEM images also showed the presence of minor cavity zones or voids on the alloys surface as in Fig. 8. These cavities may have resulted from material deformation or the presence of impurities. However, they did not appear to have a significant impact on the alloys mechanical properties, indicating its reasonable ductility and ability to withstand deformation.

4. CONCLUSION

The experimental analysis conducted on two different alloys, 77.3% Al–1.8% Fe–16.7% Si and 62.9% Al–14.4% Fe–16.9% Si, revealed significant differences in their tribological properties. The investigation involved SEM and optical micrograph of microstructure to identify wear, crack, and cavity zones. The Vickers hardness test indicated that the Al–Fe–Si alloy exhibited higher values, while the Al–Si alloy showed lower hardness, approximately 20 degrees lower.

Furthermore, in the circular wear tests conducted with different loads (3 N, 5 N, 10 N), the Al–Fe–Si alloy demonstrated less weight loss compared to the Al–Si alloy. This suggests that the former alloy has superior wear resistance under varying loads. Additionally, the roughness test results also favoured the Al–Si alloy, showing higher values compared to the Al–Fe–Si alloy, which exhibited lower and stable roughness, the findings were validated with Refs. [27–30].

Overall, the experimental findings indicate that the Al–Fe–Si alloy outperforms the Al–Si alloy in terms of hardness, and wear resistance. These results highlight the potential superiority of the first alloy, suggesting its suitability for applications requiring enhanced tribological properties. However, further investigations and tests may be required to gain a more comprehensive understanding of the alloys' behaviour under various conditions and loads, paving the way for potential engineering applications and industrial usage. The experiment could be extended to include surface modification techniques, such as coatings or treatments, to enhance the alloys' wear resistance and reduce weight loss during wear tests. This would open up possibilities for tailoring the alloys for specific applications.

REFERENCES

1. Q. Li, F. Qiu, B. X. Dong, H. Y. Yang, S. L. Shu, M. Zha, and Q. C. Jiang, *Mater. Sci. Eng. A*, **798**: 140247 (2020).
2. P. Wang, H. Lei, X. Zhu, H. Chen, and D. Fang, *J. Alloys Compd.*, **789**: 852 (2019).
3. A. M. A. Mohamed, F. H. Samuel, A. M. Samuel, and H. W. Doty, *Mater. Design*, **30**: 4218 (2009).
4. J. Xu, Y. Li, K. Ma, Y. Fu, E. Guo, Z. Chen, Q. Gu, Y. Han, T. Wang, and Q. Li, *Scripta Mater.*, **187**: 142 (2020).
5. S.-S. Li, X. Yue, Q.-Y. Li, H.-L. Peng, B.-X. Dong, T.-S. Liu, H.-Y. Yang, J. Fan, S.-L. Shu, F. Qui, and Q.-C. Jiang, *J. Mater. Research Technology*, **27**: 944 (2023).
6. K. Sunitha and K. Gurusami, *Mater. Today: Proc.*, **43**, Pt. 2: 1825 (2021).
7. L. Zhang, Z. W. Ji, J. Zhao, J. He, and H. Jiang, *Mater. Letters*, **308**: 131206 (2022).
8. L. Bolzoni, M. Nowak, and N. Hari Babu, *Mater. Design*, **66**: 376 (2015).
9. B. K. Milligan, S. Roy, C. S. Hawkins, L. F. Allard, and A. Shyam, *Mater. Sci. Eng. A*, **772**: 138697 (2020).
10. B. Li, Y. Shen, and W. Hu, *Mater. Design*, **32**: 2570 (2011).
11. V. Bharath, V. Auradi, Madeva Nagaral, Satish Babu Boppana, S. Ramesh, and K. Palanikumar, *Trans. Indian Institute of Metals*, **75**: 133 (2022).
12. M. S. Kaiser, S. H. Sabbir, M. S. Kabir, M. R. Soummo, and M. A. Nur, *Mater. Res.*, **21**, Iss. 4: e20171096 (2018).
13. C. Farsi, S. Amroune, M. Moussaoui, B. Mohamad, and H. Benkherbache, *Metallofiz. Noveishie Tekhnol.*, **41**, No. 8: 1103 (2019).
14. H. Al-Abboodi, H. Fan, M. Al-Bahrani, A. Abdelhussien, and B. Mohamad, *Facta Universitatis-Series Mechanical Engineering*, **22**: 315 (2024).
15. A. Aldeen, D. Mahdi, C. Zhongwei, I. Disher, and B. Mohamad, *Facta Universitatis-Series Mechanical Engineering*, **21**: 1 (2023).
16. N. Kang, Y. Zhang, M. El Mansori, and X. Lin, *Adv. Powder Mater.*, **2**: 100108 (2023).
17. Y. Zhang, N. Kang, M. E. Mansori, Q. Wang, J. Lu, and X. Lin, *Wear*, **522**: 204682 (2023).
18. B. Blakey-Milner, P. Gradl, G. Snedden, M. Brooks, J. Pitot, E. Lopez,

M. Leary, F. Berto, and A. du Plessis, *Mater. Design*, **209**: 110008 (2021).
19. G. P. M. Leyson, L. G. Hector Jr., and W. A. Curtin, *Acta Mater.*, **60**: 3873 (2012).
20. L. X. Xi, H. Zhang, P. Wang, H. C. Li, K. G. Prashanth, K. J. Lin, I. Kaban, and D. D. Gu, *Ceramics Int.*, **44**, Iss. 15: 17635 (2018).
21. N. Kang, M. El Mansori, X. Lin, F. Guittonneau, H. L. Liao, W. D. Huang, and C. Coddet, *Composites B: Eng.*, **155**: 382 (2018).
22. X. Wang, R. G. Guan, Y. Wang, R. D. K. Misra, B. W. Yang, Y. D. Li, and T. J. Chen, *Mater. Sci. Eng. A*, **751**: 23 (2019).
23. M. Khadem, O. V. Penkov, H. K. Yang, and D. E. Kim, *Friction*, **5**: 248 (2017).
24. A. Aversa, G. Marchese, A. Saboori, E. Bassini, D. Manfredi, S. Biamino, D. Ugues, P. Fino, and M. Lombardi, *Materials*, **12**, Iss. 7: 1007 (2019).
25. H. R. Kotadia, G. Gibbons, A. Das, and P. D. Howes, *Additive Manufacturing*, **46**: 102155 (2021).
26. X. Zhang, M. Zhang, M. Shao, X. Geng, Y. Sun, M. Niu, Y. Miao, and X. Wang, *J. Mater. Eng. Perform.*, **30**: 8030 (2021).
27. T. Rameshkumar and I. Rajendran, *Tribology Transactions*, **56**, Iss. 2: 268 (2013).
28. H. Ashrafi, M. H. Enayati, and R. Emadi, *Acta Metall. Sinica (English Letters)*, **28**: 83 (2015).
29. T. Nakase, S. Kato, T. Kobayashi, and S. Sasaki, *Proc. Institution Mechanical Eng. J: J. Eng. Tribology*, **227**, Iss. 5: 423 (2013).
30. J. Kumar, D. Singh, N. S. Kalsi, S. Sharma, C. I. Pruncu, D. Y. Pimenov, K. V. Rao, and W. Kapłonek, *J. Mater. Research Technol.*, **9**, Iss. 6: 13607 (2020).